SN 2022joj

Chang Liu [ID],[1,2] Adam A. Miller [ID],[1,2] and Fantastic Astronomers

[1] *Department of Physics and Astronomy, Northwestern University, 2145 Sheridan Rd, Evanston, IL 60208, USA*
[2] *Center for Interdisciplinary Exploration and Research in Astrophysics (CIERA), Northwestern University, 1800 Sherman Ave, Evanston, IL 60201, USA*

ABSTRACT

Keywords: Supernovae (1668), Type Ia supernovae (1728), White dwarf stars (1799), Observational astronomy (1145), Surveys (1671)

1. INTRODUCTION

2. OBSERVATIONS

2.1. *Discovery & Classification*

SN 2022joj was discovered by the Zwicky Transient Facility (ZTF; Bellm et al. 2019a; Graham et al. 2019; Dekany et al. 2020) on 2022 May 08.298 (UT dates are used throughout the paper; MJD 59707.298) with the 48 inch Samuel Oschin Telescope (P48) at Palomar Observatory. It was detected with $r_{\mathrm{ZTF}} = 19.13 \pm 0.06$ mag at $\alpha_{\mathrm{J2000}} = 14^{\mathrm{h}}41^{\mathrm{m}}40\overset{s}{.}08$, $\delta_{\mathrm{J2000}} = +03°00'24\overset{''}{.}14$ and announced to the public by Fremling (2022). The detection was made by the automatic ZTF discovery pipeline (Masci et al. 2019) with the image differencing technique (Zackay et al. 2016). A real-time alert (Patterson et al. 2019) was generated as the candidate passed internal machine-learning thresholds (e.g., Duev et al. 2019; Mahabal et al. 2019), and an internal designation ZTF22aajijjf was assigned. The last 3-σ nondetection limits the brightness to $r_{\mathrm{ZTF}} > 21.48$ mag on 2022 May 03.27 (MJD 59702.27; 5.03 days before the first detection).

The first spectrum was obtained on 2022 May 11.288 by Newsome et al. (2022), who found a best fit to a young Type I SN at $z = 0.03$ using the Supernova Identification (SNID) code (Blondin & Tonry 2007). The prominent Si II λ6355 and Ca II infrared triplet (IRT) absorption features point to a SN Ia, while the blue side of the spectrum ($\lesssim$5000 Å) is strongly suppressed (see Figure 2), atypical for a normal SN Ia at a similar phase. It was indisputably classified as a SN Ia by Chu et al. (2022) at its maximum luminosity based on its blue color and persistent Si II features.

2.2. *Host Galaxy*

The host of SN 2022joj is a dwarf galaxy at $\alpha_{\mathrm{J2000}} = 14^{\mathrm{h}}41^{\mathrm{m}}40\overset{s}{.}04$, $\delta_{\mathrm{J2000}} = +03°00'24\overset{''}{.}53$, cataloged in the DESI Legacy Survey (LS; Dey et al. 2019). SN 2022joj has a projected offset of only $0\overset{''}{.}5$ to the host. On 2023 April 26, we took a spectrum of both the SN and the host using the Low Resolution Imaging Spectrometer (LRIS) on the Keck I 10m telescope (Oke et al. 1995). We placed the slit across both the center of the galaxy and the position of the SN (Figure 3), with a total integration time of 3600 s. The spectrum was reduced with the PypeIt package (Prochaska et al. 2020). While the continuum spectrum of the host was still outshined by the SN, we detected a potential host emission line at 6742.4 Å with a signal-to-noise ratio (S/N) of $\sim$5. If this is associated with the Hα emission, the corresponding redshift of the host galaxy is $z = 0.02736$, which is in general agreement with the estimated value $z = 0.03$ by matching the SN spectra to SNID templates (Newsome et al. 2022). In the 2D spectrum (Figure 3), the trace is dominated by the light of the SN in the nebular phase, while the center of this emission feature has a offset of $\sim$3–4 pixels to the center of the trace. The CCDs equipped on LRIS have a pixel scale of $0\overset{''}{.}135$/pixel, so this offset corresponds to an angular offset of $\sim 0\overset{''}{.}4$–$0\overset{''}{.}5$, consistent with the archival value. This indicates that the Hα detection should not be an artifact.

We estimate the distance modulus of SN 2022joj in the following way. We first use the 2M++ model (Carrick et al. 2015) to estimate the peculiar velocity of the host galaxy to be 383 ± 250 km s^{-1}. Then the peculiar velocity is combined with the recession velocity in the frame of the cosmic microwave background (CMB) $v_{\mathrm{CMB}} = 8424$ km s^{-1}, which yields a net Hubble recession rate of 8193 ± 250 km s^{-1}. Using cosmological parameters $H_0 = 70$ km s^{-1} Mpc^{-1}, $\Omega_M = 0.3$, and $\Omega_{\Lambda} = 0.7$, the estimated luminosity distance to SN 2022joj is 119.5 Mpc, equivalent to a distance modulus of 35.39 ± 0.03 mag.

Table 1. Basic photometric properties of SN 2022joj.

	g_{ZTF}	r_{ZTF}	B
t_{max} (MJD)	59723.94 ± 0.02	59725.03 ± 0.02	59723.14 ± 0.02
M_{max} (mag)	-19.698 ± 0.005	-19.429 ± 0.002	-19.822 ± 0.007
t_{fl} (MJD)		$59702.75^{+0.86}_{-0.67}$	
α		$2.32^{+0.23}_{-0.29}$	
$t_{\mathrm{fl},\alpha=2}$ (MJD)		$59703.65^{+0.10}_{-0.11}$	

NOTE—Properties at maxnium are estimated in a SALT3 (Kenworthy et al. 2021) fit with the package sncosmo (Barbary et al. 2023), while t_{fl} and α are estimated in power-law fits to r_{ZTF} early light curves. The absolute magnitudes have been corrected for Galactic extinction.

2.3. *Optical Photometry*

SN 2022joj was monitored in g_{ZTF}, r_{ZTF}, and i_{ZTF} by ZTF as part of its ongoing Northern Sky Survey (Bellm et al. 2019b), while the i_{ZTF} data only cover the decline from the peak. We adopt a Galactic extinction of $E(B-V)_{\mathrm{MW}} = 0.032\,\mathrm{mag}$ (Schlafly & Finkbeiner 2011), and correct all photometry using the extinction model from Fitzpatrick (1999) assuming $R_V = 3.1$. We do not find any Na I D absorption at the redshift of the host galaxy, indicating that the extinction from the host is negligible. The blue $g_{\mathrm{ZTF}} - r_{\mathrm{ZTF}}$ color ($\sim -0.2\,\mathrm{mag}$) near maximum luminosity after correcting for the Galactic extinction is also consistent with no additional reddening from the host. Therefore we assume $E(B-V)_{\mathrm{host}} = 0$.

The basic photometric properties of SN 2022joj are listed in Table 1. We do not include the maximum i_{ZTF}-band properties, which are relatively uncertain due to the low cadance in i_{ZTF} around peak. The forced-photometry light curves[1] in g_{ZTF} and r_{ZTF} (in absolute magnitudes) are shown in Figure 1. These light curves are reduced using the pipeline from A. A. Miller et al. (2023, in preparation); see also Yao et al. (2019).

2.4. *Optical Spectroscopy*

We obtained a series of optical spectra of SN 2022joj using the Spectral Energy Distribution Machine (SEDM; Blagorodnova et al. 2018) on the automated 60 inch telescope (P60; Cenko et al. 2006) at Palomar observatory, the Andalucia Faint Object Spectrograph and Camera (ALFOSC)[2] installed at the Nordic Optical Telescope (NOT), the SPectrograph for the Rapid Acquisition of Transients (SPRAT; Piascik et al. 2014) on the 2 m Liverpool Telescope (LT; Steele et al. 2004),

[1] https://web.ipac.caltech.edu/staff/fmasci/ztf/forcedphot.pdf
[2] http://www.not.iac.es/instruments/alfosc/

Table 2. Spectroscopic observations of SN 2022joj.

t_{obs}	Phase	Telescope/	R	Range
(MJD)	(days)	Instrument	$(\lambda/\Delta\lambda)$	(Å)
59,710.29	-12.5	FTN/FLOYDS-N	550	3500–10000
59,725.34	$+2.2$	P60/SEDM	100	3770–9220
59,725.43	$+2.2$	P60/SEDM	100	3770–9220
59,732.02	$+8.7$	NOT/ALFOSC	360	3500–9700
59,744.96	$+21.3$	LT/SPRAT	350	4020–7990
59,752.50	$+28.6$	FTS/FLOYDS-S	550	3500–10000
59,759.92	$+35.8$	LT/SPRAT	350	4020–7990
59,760.37	$+36.3$	Keck I/LRIS	1100	3100–10280
59,784.89	$+60.1$	NOT/ALFOSC	360	3850–9620
60,017.42	$+286.5$	MMT/Binospec	1340	3830–9210
60,061.56	$+329.4$	Keck I/LRIS	1100	3200–10150

NOTE—Phase is measured relative to the B-band peak in the rest frame of the host galaxy. The resolution R is reported for the central region of the spectrum.

FLOYDS spectrograph[3] on the 2m Faulkes Telescope South (FTS) at Siding Spring as part of the Las Cumbres Observatory global telescope (LCOGT) network (Brown et al. 2013), Binospec (Fabricant et al. 2019) on the 6.5m MMT telescope, and LRIS on the Keck I 10m telescope (Oke et al. 1995). With the exception of observations obtained with SEDM, all spectra were reduced using standard procedures (e.g., Matheson et al. 2000). The SEDM spectra were reduced using the custom pysedm software package (Rigault et al. 2019). Details of the spectroscopic observations are listed in Table 2. The resulting spectral sequence is shown in Figure 2. All the spectra listed in Table 1 will be available on WISeREP (Yaron & Gal-Yam 2012).

We also include the spectrum uploaded to the Transient Name Server (TNS) by Newsome et al. (2022) in our analysis, which was obtained using the FLOYDS spectrograph on the 2m Faulkes Telescope North (FTN) at Haleakala.
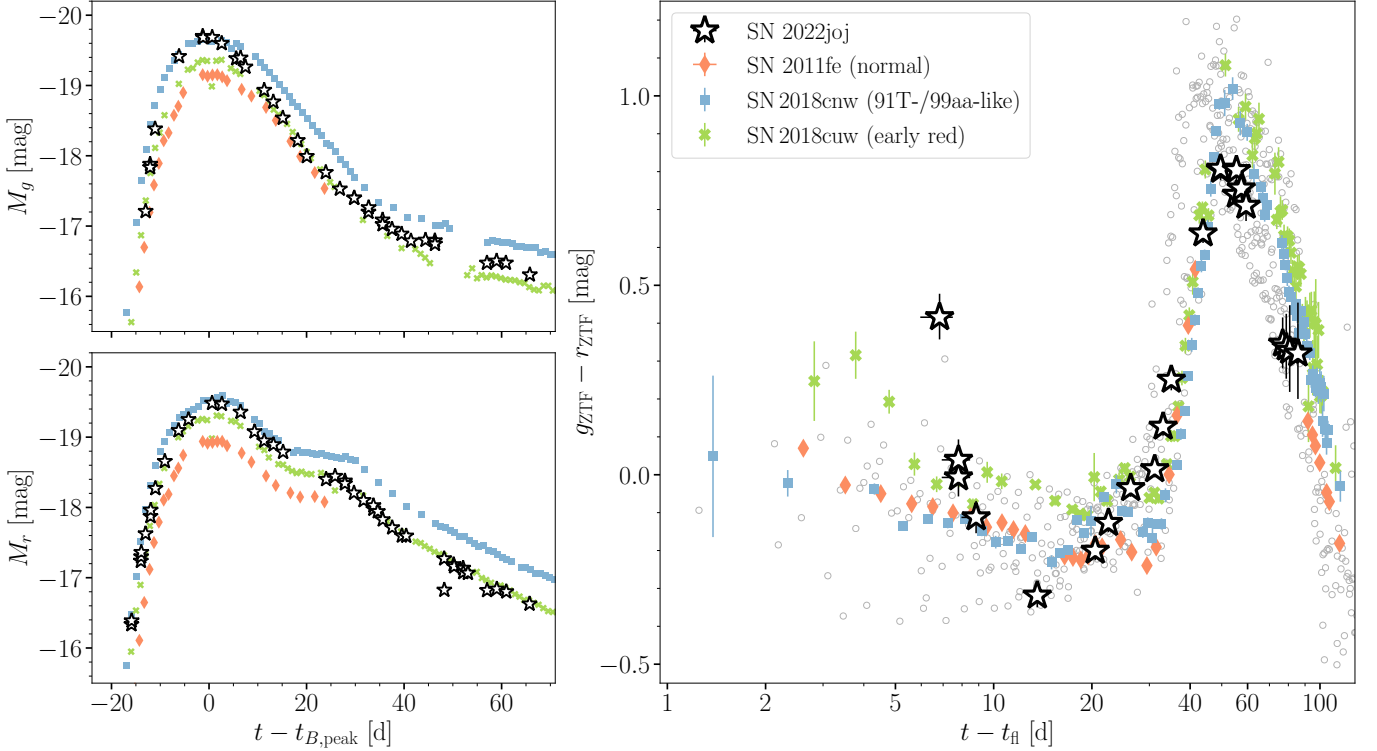
3. ANALYSIS

3.1. *Early Light Curves and the First Light*

To estimate the time of first light (t_{fl}), we follow the convention (e.g., Miller et al. 2020) by assuming a power-law rise in the broad-band flux $f(t)$,

$$f(t) = A(t - t_{\mathrm{fl}})^{\alpha},$$

where A is a constant amplitude and α is the power-law index. In practice we only fit the r_{ZTF}-band forced-

[3] https://lco.global/observatory/instruments/floyds/

Figure 1. Comparison of the photometric properties of SN 2022joj with those of SN 2011fe (normal Ia; Pereira et al. 2013), SN 2018cnw (91T-/99aa-like), and SN 2018cuw (normal Ia with a red early color). *Left*: multiband light curves. The upper (lower) panel shows the evolution in the g-band (r-band) absolute magnitude. *Right*: $g_{ZTF} - r_{ZTF}$ color evolution. The gray circles denote the color evolution of 14 nearby ($z \leq 0.05$) SNe Ia (open circles) from the ZTF sample with prompt observations within 5 days of first light (Bulla et al. 2020). Note that we have not performed K-corrections, so all the SNe were observed at slightly different filters.

photometry light curve, since we do not have any early detection in i_{ZTF}, and the g_{ZTF}-band flux is strongly suppressed at the early phase (see Section 3.2). We estimate α, t_{fl}, and $\ln A$ in a Bayesian approach by sampling their posterior distributions with Markov Chain Monte Carlo (MCMC) using the package PyMC (Salvatier et al. 2016). We find that the r_{ZTF}-band light curve is consistent with a power-law rise with $\alpha = 2.32^{+0.23}_{-0.29}$, in which the first detection in r_{ZTF} is $4.55^{+0.86}_{-0.67}$ days after the first light. This estimate is still consistent with the $\alpha = 2$ fireball model. When fixing $\alpha = 2$, the model still fits the light curve well, but the estimated t_{fl} is ∼1 day later (see Table 1). We do not find any correlated residuals as evidence for a flux excess in r_{ZTF} after ∼5 days since t_{fl}, although a flux excess before the first detection could not be ruled out.

3.2. *Photometric Properties*

SN 2022joj shows a few peculiar photometric features compared to normal SNe Ia. In Figure 1, we compare the g_{ZTF}, r_{ZTF} light curves and the $g_{ZTF} - r_{ZTF}$ color evolution of SN 2022joj with those of the well-observed

normal SN Ia, SN 2011fe,[4] as well as SN 2018cnw (ZTF18abauprj) and SN 2018cuw (ZTF18abcflnz) from a sample of SNe Ia with prompt observations within 5 days of first light by ZTF (Yao et al. 2019; Bulla et al. 2020). SN 2018cnw is an overluminous SN Ia that falls into the category of SN 1999aa-like (99aa-like; Garavini et al. 2004) or SN 1991T-like (91T-like; Filippenko et al. 1992a) objects, while SN 2018cuw is a normal SN Ia with a red $g_{ZTF} - r_{ZTF}$ color comparable to that of SN 2022joj at early time.

Around maximum brightness, SN 2022joj is overluminous, comparable to SN 2018cnw, and ∼0.5 mag brighter than SN 2011fe in both g_{ZTF} and r_{ZTF}. But SN 2022joj clearly stands out due to its fast evolution in g_{ZTF}. While SN 2022joj and SN 2018cnw show a similar maximum brightness in g_{ZTF}, upon the earliest detection in g_{ZTF} at ∼−13 days, the corresponding absolute magnitude (-17.2 mag) is ∼0.8 mag fainter than

---

[4] we adopt the synthetic photometry in g_{ZTF} and r_{ZTF} calculated using the spectrophotometric sequence from Pereira et al. (2013)
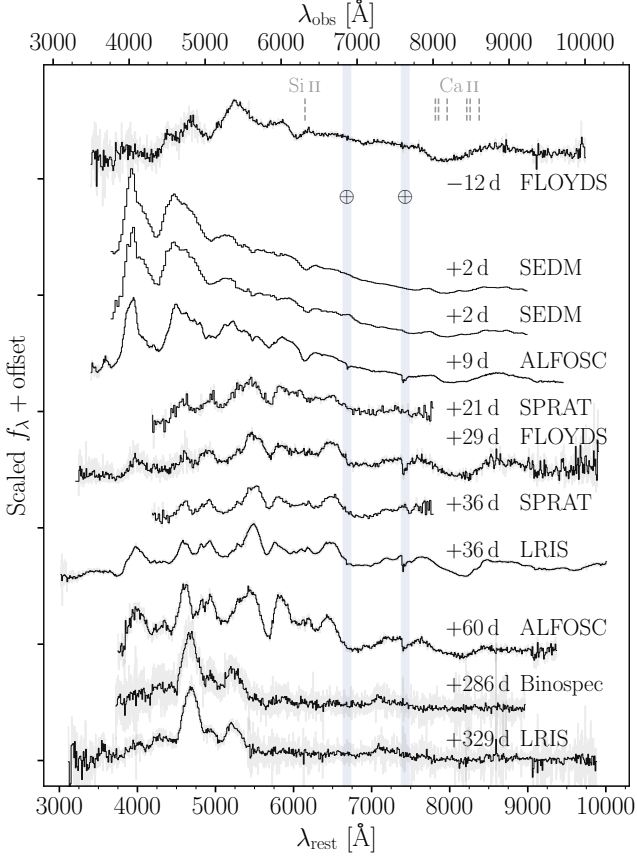
Figure 2. Optical spectral sequence of SN 2022joj. Rest-frame phases (days) relative to the *B*-band peak and instruments used are posted next to each spectrum. Spectra have been corrected for $E(B - V)_{\rm MW} = 0.032$ mag and are shown in gray. The black lines are binned spectra with a bin size of 10 Å, except for the SEDM spectra, whose resolution is lower than the bin size. The corresponding wavelengths of the Si II λ6355 line (with an expansion velocity of $10{,}000 \,{\rm km\,s^{-1}}$) and the Ca II IRT (with expansion velocities of both $10{,}000 \,{\rm km\,s^{-1}}$ and $25{,}000 \,{\rm km\,s^{-1}}$) are marked by the vertical dashed lines. The strong optical telluric features are marked by the blue shaded region.

that of SN 2018cnw at a similar phase. This means on average, SN 2022joj rises faster than SN 2018cnw by $\sim$0.06 mag day^{-1} in $g_{\rm ZTF}$ during that period of time. On the decline, the $\Delta m_{15}(g_{\rm ZTF})$ of SN 2022joj is $\sim$1.2 mag, which is significantly greater than that of the overluminous SN 2018cnw ($\Delta m_{15}(g_{\rm ZTF}) \simeq 0.7$ mag) or normal SN 2011fe ($\Delta m_{15}(g_{\rm ZTF}) \simeq 0.8$ mag). This is atypical for overluminous SNe Ia, which are among the slowest decliners in the SN Ia population (Phillips et al. 1999; Taubenberger 2017). Such a rapid decline is probably due to a quickly developing exotic absorption feature near 4200 Å (see Section 3.3). In $r_{\rm ZTF}$ its behavior near maximum is generally similar to other SNe Ia, although the evolution still appears slightly faster.

The trail of SN 2022joj on the color evolution diagram does not overlap with any normal SNe Ia, as shown in the right panel of Figure 1. We overplot 14 nearby ($z \lesssim 0.05$) normal and 99aa-/91T-like SNe Ia from the ZTF early Ia sample (Bulla et al. 2020). They are corrected for Galactic extinction, but *K*-corrections have not been performed for consistency. Given the indisputable photometric and spectroscopic peculiarities in SN 2022joj, we do not expect any softwares trained on samples of normal SNe Ia would be able to estimate its *K*-correction correctly. Nevertheless, given its relatively low redshift ($z \lesssim 0.03$), the *K*-correction is not expected to be huge. For the same reason we only include a subset of low-redshift SNe Ia from the sample of Bulla et al. (2020). SN 2022joj is remarkably red ($g_{\rm ZTF} - r_{\rm ZTF} \simeq 0.4$ mag) around $\sim$7 days after $t_{\rm fl}$, and is clearly an outlier compared to the normal Ia sample. In the following week, SN 2022joj quickly turns into blue, and is among the bluest objects in the sample $\sim$15 days after $t_{\rm fl}$. SN 2018cuw has a comparable $g_{\rm ZTF} - r_{\rm ZTF}$ color at early times, but shows a much slower blueward evolution afterwards. From $\sim$10–20 days after $t_{\rm fl}$, before its reaches maximum brightness, SN 2022joj starts to evolve redward in the next $\sim$2 months, qualitatively similar to other SNe Ia. While the overall trend resembles that of other SNe Ia, the turning point comes $\sim$20 days earlier. Due to its rapid decay in $g_{\rm ZTF}$ after maximum brightness, it appears redder than the normal SN 2011fe, the overluminous SN 2018cnw, and the early-red object SN 2018cuw $\sim$30–40 days after $t_{\rm fl}$. When $g_{\rm ZTF} - r_{\rm ZTF}$ reaches maximum ($\sim$0.8 mag), SN 2022joj is again bluer than most of the SNe Ia in the ZTF sample. Eventually as SN 2022joj steps into the transitional phase, its color evolution follows the Lira law[5] (Lira 1996; Phillips et al. 1999) and shows no significant difference from that of SNe Ia.

To conclude, despite of its similarity in luminosity and color to 99aa-like/91T-like events at maximum brightness, the rapid rise and decline in light curves and the bizarre color evolution both indicate that SN 2022joj exhibits much more peculiarities compared to normal SNe Ia.

3.3. *Optical Spectral Properties*

In Figure 2, we show the optical spectral sequence of SN 2022joj. The earliest spectrum obtained by Newsome et al. (2022) $\sim$12 days before maximum brightness

---

[5] The original Lira law was discovered in $B - V$ color. But in the $g_{\rm ZTF} - r_{\rm ZTF}$ color we see a similar trend.
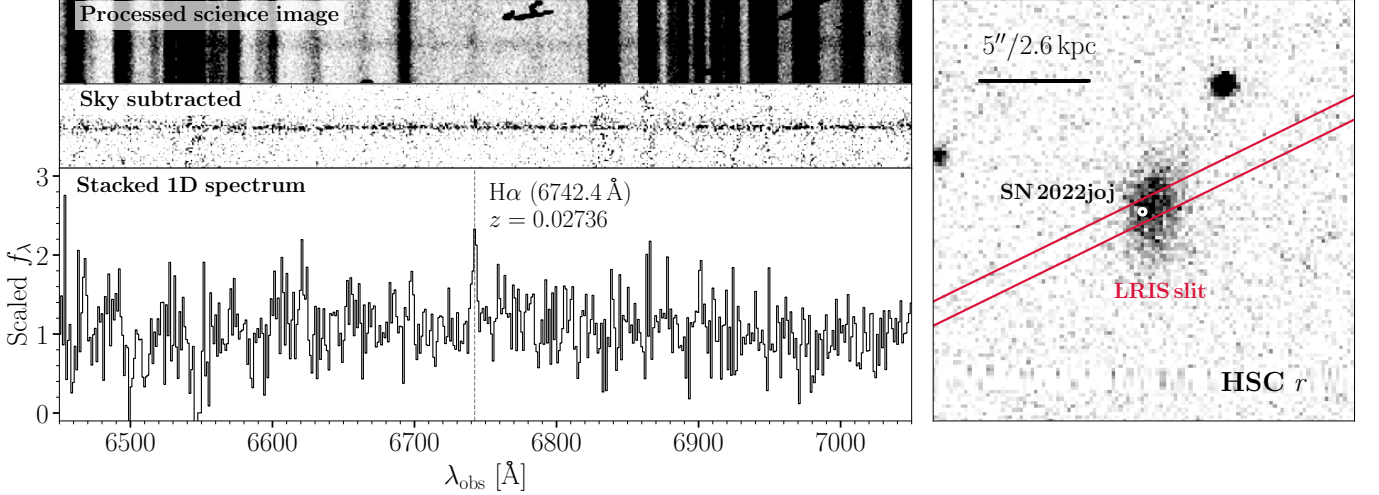
Figure 3. The LRIS spectrum reveals an Hα emission line from the host galaxy at 6742.4 Å, corresponding to a redshift $z = 0.02736$. *Left:* the Hα emission in the observed 2D and 1D spectrum. *Right:* the offset of SN 2022joj to the host galaxy and how the slit was placed when obtaining the LRIS spectrum.

Table 3. Fits to the expansion velocities and pEWs of Si II λλ5972, 6355 and the Ca II IRT of SN 2022joj.

	Si II λ5972		Si II λ6355		Ca II IRT, PVFs		Ca II IRT, HVFs	
Phase	v	pEW	v	pEW	v	pEW	v	pEW
(day)	$(10^3\,\mathrm{km\,s^{-1}})$	(Å)	$(10^3\,\mathrm{km\,s^{-1}})$	(Å)	$(10^3\,\mathrm{km\,s^{-1}})$	(Å)	$(10^3\,\mathrm{km\,s^{-1}})$	(Å)
−12.5	⋯	⋯	−15.66 ± 0.13	47.5 ± 2.5	−14.85 ± 0.83	190 ± 34	−25.98 ± 0.56	278 ± 40
+2.2	−8.77 ± 0.63	2.9 ± 1.5	−10.28 ± 0.13	27.8 ± 1.3	−12.03 ± 0.73	58 ± 11	−22.51 ± 0.33	109 ± 11
+2.3	−8.35 ± 0.62	4.4 ± 2.6	−9.87 ± 0.28	25.4 ± 2.7	−11.77 ± 0.93	85 ± 17	−22.17 ± 0.47	105 ± 15
+8.7	⋯	⋯	−10.37 ± 0.04	48.5 ± 0.6	−12.07 ± 0.25	147 ± 7	−21.21 ± 0.16	124 ± 7

exhibits prominent absorption lines associated with Si II λ6355 and Ca II IRT. It also shows a strong suppression of flux blueward of ∼5000 Å, which accounts for the unusually red color of SN 2022joj at early times. Near maximum brightness, the two SEDM spectra show a very blue continuum between ∼5000–8000 Å with shallow absorption features, indicating a high photometric temperature. Si II λλ5972, 6355 lines, the S II W-trough, and Ca II IRT are detectable but not prominent. A wide, asymmetric absorption feature appears between ∼4000–4500 Å (the 4200 Å features hereafter). There is a break on the blue edge of this feature which could be associated with Si II λ4128 that is widely seen in other SNe Ia. However, the spectra of most of the normal and overluminous 99aa-like/91T-like SNe Ia show another peak at ∼4100–4200 Å redward of a narrow Si II λ4128 feature, which is absent in the spectra of SN 2022joj. The 4200 Å features become even wider and deeper in the ALFOSC spectrum at ∼+9 days. Weeks after the maximum, in the FLOYDS spectrum (+29 days) and the

LRIS spectrum (+36 days), the bottom of the 4200 Å features becomes flat, reminiscent of the Ti-trough in the subluminous SN 1991bg-like (91bg-like; Filippenko et al. 1992b; Leibundgut et al. 1993). The nebular-phase spectra are dominated by [Fe II], [Fe III], and [Co III] emission lines, but the [Fe II] features (e.g, the complex around ∼7300 Å) appear weaker than those in other SNe Ia, probably suggesting a high ionization in the ejecta. We will discuss the late-time spectra of SN 2022joj in detail in Section 4.2.

In Figure 4, we compare the optical spectra of SN 2022joj to those of some other SNe Ia during photospheric and transitional phases. Near peak, the blue continuum in the spectrum of SN 2022joj and shallow absorption lines are both similar to those of overluminous objects, including SN 1991T, SN 1999aa, and SN 2000cx. The asymmetric 4200 Å features are not seen in SN 1991T or SN 1999aa, while in SN 2000cx, a similar (but narrower) absorption feature is interpreted as high velocity Ti II (Branch et al. 2004). The 4200 Å fea-
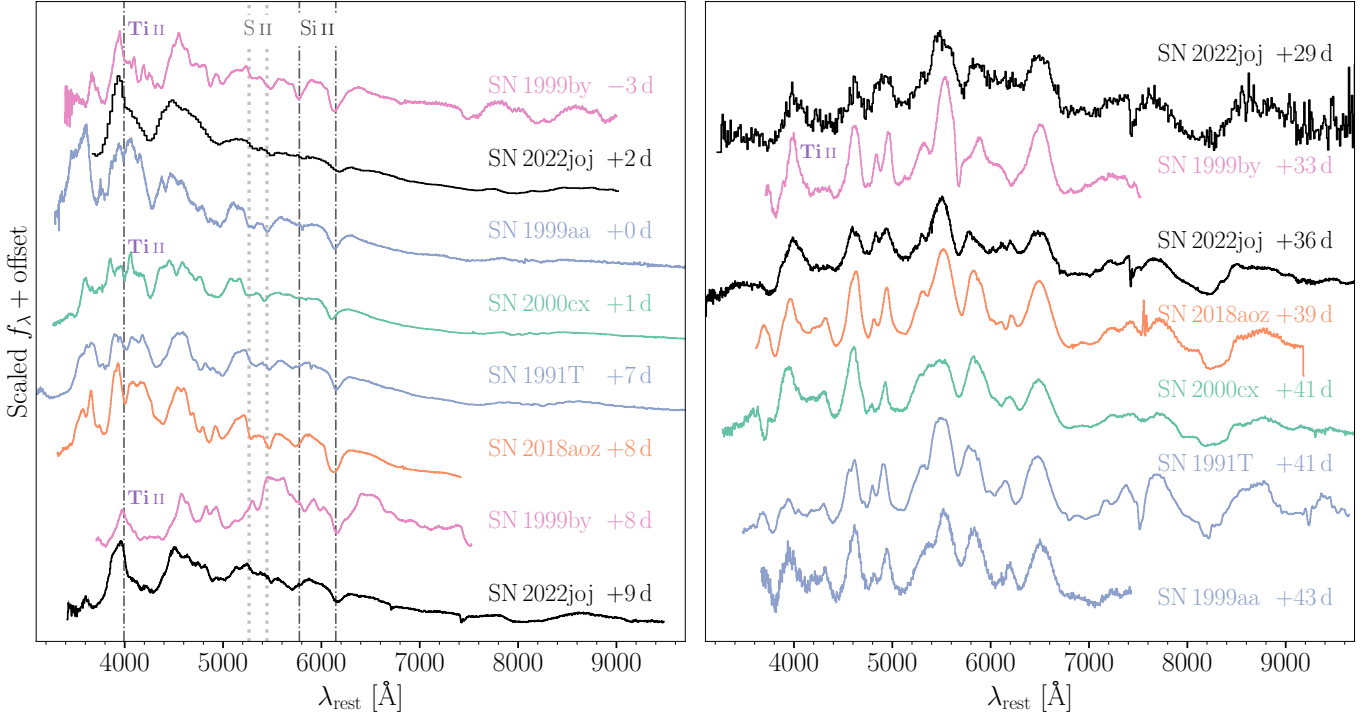
Figure 4. Optical spectra of SN 2022joj (black) and (i) a subluminous SN Ia, SN 1999by (magenta), (ii) two overluminous SNe Ia, SN 1991T and SN 1999aa (blue), (iii) an overluminous SN with exotic Ti II features in the spectrum, SN 2000cx (green), and (iv) a normal SN Ia with a red color at early time, SN 2018aoz (orange), near maximum brightness (left panel) and a month after maximum (right panel). The dash-dotted lines correspond to wavelengths of three Si II lines (4128 Å, 5972 Å, and 6355 Å), while the dotted lines correspond to the wavelengths of the S II W-trough (both assuming an expansion velocity of 10,000 km s^{-1}). Ti II has been identified from the spectra of SN 1999by and SN 2000cx at around ~4200 Å, and the corresponding features are labeled. We obtain the spectra of these SNe Ia from Matheson et al. (2008) (SN 1999by) and Silverman et al. (2012) (SN 1991T, SN 1999aa, and SN 2000cx) except for SN 2018aoz, whose spectra are obtained from Ni et al. (2023).

tures are actually much more similar to the well-known Ti-trough that is ubiquitous in subluminous 91bg-like objects, e.g., SN 1999by (Arbour et al. 1999). Prior to the peak, SN 1999by also shows this asymmetric absorption at about the same wavelength. A week after the maximum, this absorption feature has been widen and appears as a flat trough, which results from a blend of multiple IGEs dominated by Ti II (Filippenko et al. 1992b; Mazzali et al. 1997). It remains prominent in the spectrum a month after the maximum. Similarly, we find that this trough is prominent in the spectra of SN 2022joj at +29 days and +36 days. Other normal/overluminous SNe Ia, unlike SN 2022joj, all exhibit a dip around ~4500 Å. Nevertheless, aside from the 4200 Å features, SN 2022joj is by no means similar to 91bg-like objects, which are ≳2 mag fainter at peak and exhibit much stronger Si II, Ca II and O I from a cooler line-forming region (Filippenko et al. 1992b). Ironically, the Ti-trough is also interpreted as a result of a low photospheric temperature (Mazzali et al. 1997). Whether the 4200 Å features in SN 2022joj are dominated by Ti II remains to be questioned.

SN 2022joj also shows remarkably shallow Si II absorption at maximum brightness. Following the techniques elaborated in Liu et al. (2023), we fit the Si II features with multiple Gaussian profiles. In Table 3 we list the estimates of the expansion velocities and the pseudo-equivalent widths (pEWs) of the major absorption lines from ~−12 days to ~+9 days. In Figure 5 we show the maximum brightness in B and properties of the Si II features for SN 2022joj, compared to those of a sample of normal SNe Ia from Zheng et al. (2018) and Burrow et al. (2020). This plot again shows that SN 2022joj is slightly overluminous and has a relatively low expansion velocity measured with the Si II λ6355 line (hereafter $v_{\rm Si}$). The pEWs in both Si II λ6355 and Si II λ6355 lines in SN 2022joj are lower than most of the normal SNe Ia, placing SN 2022joj to an extreme of the shallow-silicon group proposed in Branch et al. (2006), which mainly consists of overluminous 91T-like/99aa-like objects. This is consistent with the high luminosity and the blue color of SN 2022joj, since a high photometric temperature promotes the average ionization level of Si, reducing the abundance of singly ionized atoms.
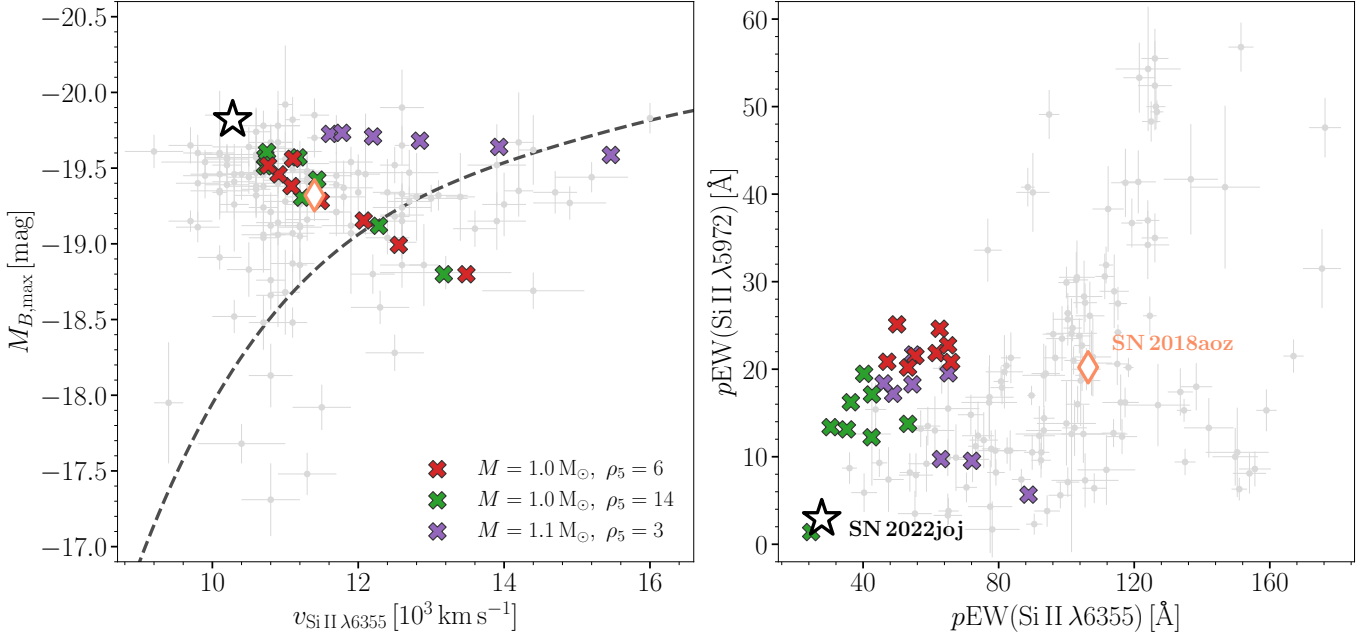
Figure 5. SN 2022joj (black star) as an overluminous SN Ia marked by its shallow Si II features. *Left:* the *B*-band absolute magnitude versus the expansion velocity of Si II λ6355 at maximum brightness. *Right:* the pseudo-equivalent width (pEW) of the two Si II lines, Si II λλ5972, 6355, at maximum brightness. The grey dots are the normal SNe Ia sample adopted from Zheng et al. (2018) and Burrow et al. (2020). The crosses of a color show where the 2D DDet models from Shen et al. (2021b) with one specific model setup would be in the parameter space. Three types of setups are included. The scattering within models with the same setups are due to different viewing angles, from $\mu = -0.93$ to $\mu = +0.93$. Parameters of the potential DDet normal SN Ia, SN 2018aoz, are also overplotted as an orange diamond.

Interestingly, the *p*EW of Si II λ6355 near peak is significantly lower than that in the first spectrum. In typical 91T-like/99aa-like objects, the Si II features are relatively weak or even undetectable at early times, when the ejecta are even hotter, and only start to emerge around maximum light (Filippenko et al. 1992a). In the early spectrum of SN 2022joj, in contrast, stronger absorption features from singly charged Si and Ca indicate a cooler line-forming region at early time compared to that near maximum brightness.

In conclusion, the spectral evolution of SN 2022joj shows some similarities to those of 91T-like/99aa-like objects, as well as exotic peculiarities. A reasonable explosion model need to reproduce (i) strong suppression in flux blueward of ∼5000 Å at early times, and a rapid blueward evolution afterwards; (ii) the seemingly contradictory observables at peak, namely the tentative Ti II features and the blue continuum/shallow Si II feature at maximum, which usually indicate low and high photometric temperatures, respectively.

4. DISCUSSION

4.1. *Models*

SNe Ia are generally expected to show a blue color shortly after its explosion when the hot ejecta have not yet cooled down. In addition, when there is an external energy source (e.g., shocks), the SN can show an excess in flux in the early light curves that appears even bluer. A non-negligible fraction of SNe Ia exhibit a blue flux excess (Deckers et al. 2022) Interactions of the ejecta with either a non-degenerate companion star (Cao et al. 2015; Marion et al. 2016; Hosseinzadeh et al. 2017) or some dense circumstellar material (Jiang et al. 2021; Dimitriadis et al. 2023) could produce such a flux excess during shock cooling. Other scenarios include the presence of ^{56}Ni in the outermost ejecta due to mixing (Piro & Nakar 2013; Magee & Maguire 2020), or as the products in the detonation of a helium shell (Polin et al. 2019).

However, there are not many scenarios that could possibly lead to a red color in the early light curve of a SN Ia when the ejecta are still hot and dense, as is the case of SN 2022joj. If the ^{56}Ni synthesized at the center of the WD is not mixed with the outer layers and remains confined, the outer ejecta, where the ^{56}Ni heating has yet to reach, will quickly cool down as they expand adiabatically at early times (Piro & Morozova 2016). In the model with no ^{56}Ni in Piro & Morozova (2016), for the ∼6 days after the explosion the SN is expected to show an extremely red $B - V$ color (see their Figure 8), before the photosphere moves in to where the ejecta have been significant heated up by ^{56}Ni. However, models
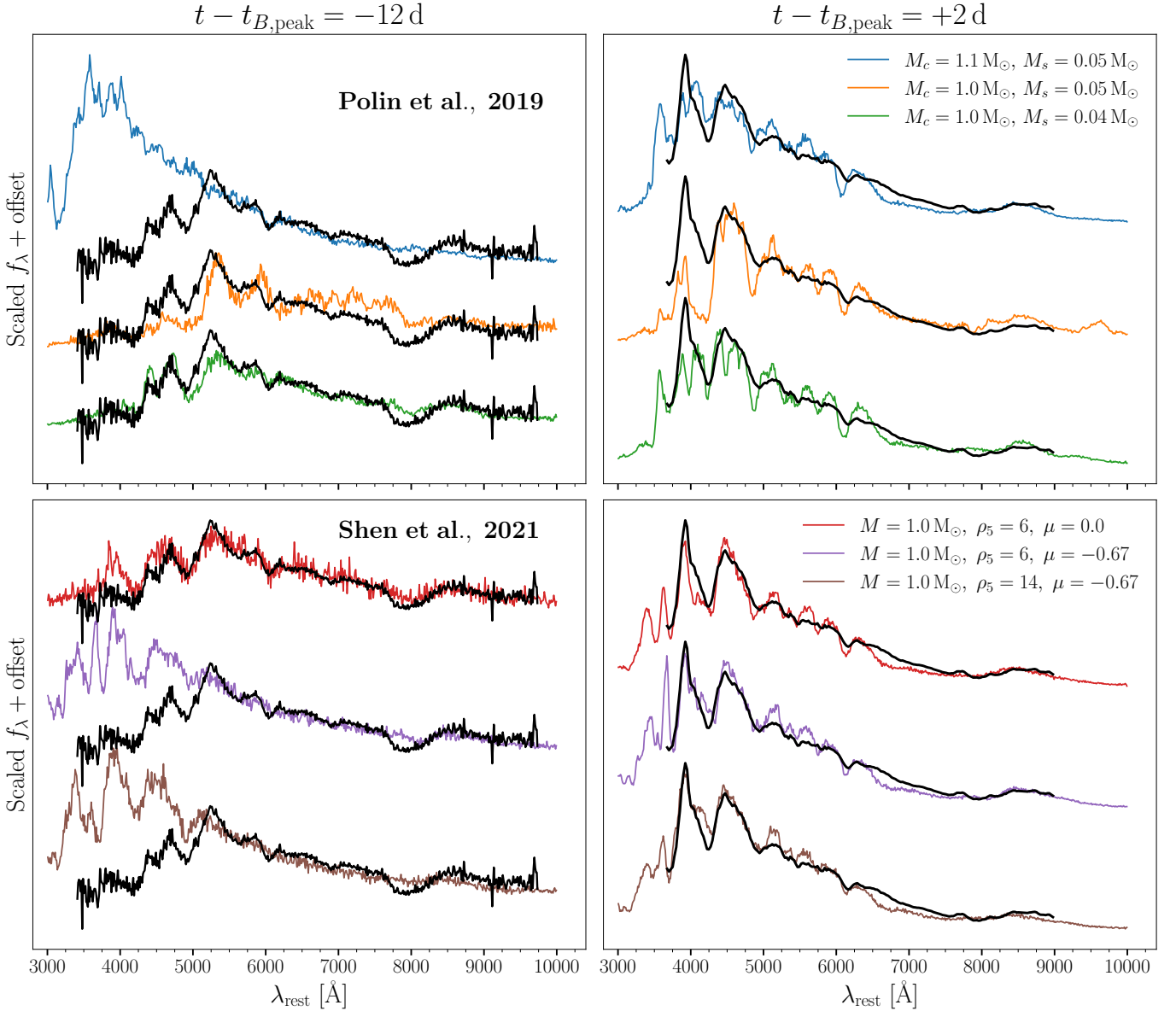
Figure 6. Comparisons of an early spectrum (~-12 days) and a maximum-light spectrum ($\sim+2$ days) of SN 2022joj (black) with two sets of DDet models at corresponding phases. *Top:* results of 1D hydrodynamical simulations from Polin et al. (2019) with a variety of core masses (M_c) and shell masses (M_s). *Bottom:* results of 2D hydrodynamical simulations from (Shen et al. 2021b) with different total masses (M), densities at the bottom of the helium shell (ρ_5 in units of $10^5 \, \mathrm{g\,cm^{-3}}$), and viewing angles ($\mu$ defined as the cosine of the polar angle relative to the point where the helium-shell detonation occurs). A Galactic extinction of $E(B-V)_{\mathrm{MW}}$ has been applied to each synthetic spectrum.

with different degrees of mixing appear similar after the first ~6 days. In addition, models with a low degree of mixing are expected to have a "dark phase" (Piro & Nakar 2013) between the explosion and the first light of ~1–5 days, which roughly accounts for the escaping timescale of the photons emitted by the ^{56}Ni underneath through diffusion. If the progenitor of SN 2022joj really has an extremely confined ^{56}Ni distribution, then when we had our first color measurement ~7 days after t_{fl}, the time since the explosion could be even longer, say,

~10 days. At this phase, even the model with the most confined ^{56}Ni distribution in Piro & Morozova (2016) has turned into a normal blue color, while we still see an unusually red color in SN 2022joj. On the other hand, it has also been shown in Piro & Morozova (2016) that the early light curves of the normal object SN 2011fe is consistent with a non-negligible level of ^{56}Ni mixing in the ejecta. It remains to be questioned whether there is an explosion scenario in which ^{56}Ni does not get mixed at all.

Alternatively, in the DDet scenario, a layer of iron-group elements (IGEs) in the ashes of the helium shell can blanket the UV photons from the bulk ejecta, causing a red color (Polin et al. 2019). This scenario has been proposed for a few archived objects with a red flux excess in their early light curves, including SN 2016jhr (Jiang et al. 2017) and SN 2018aoz (Ni et al. 2022). In Figure 6 we compare the spectra of SN 2022joj at ~-12 days and near the maximum with those of DDet models in Polin et al. (2019) and Shen et al. (2021b). Models from Polin et al. (2019) are based on 1D hydrodynamical simulations, while 2D simulations are performed in models from Shen et al. (2021b). To create synthetic spectra, both models use the multi-dimensional radiative transfer `Sedona` code assuming local thermodynamical equilibrium (LTE). We refer to them as 1D models and 2D models hereafter, respectively.

In the 1D models, the prime model parameters are the mass of the C/O core (M_c) and the mass of the helium shell (M_s). The maximum luminosity depends on the amount of ^{56}Ni synthesized in the explosion, which is essentially determined by the total progenitor mass (M_c+M_s) in 1D models (Polin et al. 2019). We find that the maximum brightness in B ($M_{B,\max} = -19.82$ mag) is reproduced by the 1D models with relatively massive progenitors ($\sim 1.2\,M_\odot$). However, models with such massive progenitors tend to produce blue, featureless spectra at early times (e.g., the $M_c = 1.1\,M_\odot$, $M_s = 0.05\,M_\odot$ model in Figure 6), inconsistent with the observations. Less massive models could reproduce the line-blanketing features in the early spectra, but fail to reproduce the maximum brightness as well as the 4300 Å features in the observed spectra. In addition, all these 1D models overestimate the strength and the expansion velocity of the Si II λ6355 line at peak.

The tension in the line strengths and velocities can be mitigated by accounting for viewing angle effects in multi-dimensional models. In Figure 5 we overplot the properties of a few 2D DDet models from Shen et al. (2021b) of different total progenitor masses M and densities at the bottom of the helium shell ρ_5 (in units of $10^5\,\mathrm{g\,cm^{-3}}$). We obtain the Si II line properties with the same fitting techniques in Section 3.3. We again find that more massive progenitors generally lead to brighter events, but with the same model setups, there is significant scattering due to different viewing angles. In the plot, the cosine value of the polar angle relative to the point of helium detonation, μ, ranges from $+0.93$ (near the helium detonation) to -0.93 (opposite to the helium detonation). When the SN is observed along a line of sight closer to the detonation point in the shell (greater μ), it will appear fainter at maximum brightness and

show a higher line velocity in Si II λ6355. We overplot the theoretical $M_{B,\max}$-v_{Si} relation of 1D DDet models across a spectrum of progenitor masses in Polin et al. (2019) as the dashed black curve. For a relatively high progenitor mass ($\gtrsim 1.1\,M_\odot$), a high v_{Si} ($\gtrsim 13{,}500\,\mathrm{km\,s^{-1}}$) is predicted. However, with $\mu \lesssim 0$, all the 2D models show a lower v_{Si} ($\lesssim 12{,}000\,\mathrm{km\,s^{-1}}$), much closer to SN 2022joj in the $M_{B,\max}$-v_{Si} phase space. Models with $\mu > 0$ are more consistent with the predictions in 1D models. It has been argued that the high-velocity SNe Ia that generally follow the theoretical $M_{B,\max}$-v_{Si} relation of 1D DDet models likely originate from sub-M_{Ch} WDs triggered by DDet, while the SNe Ia in the clump centered at $M_{B,\max} \simeq -19.5$ mag and $v_{\mathrm{Si}} \simeq 11{,}000$ kms are candidates of near-M_{Ch} explosions (Polin et al. 2019; Nugent et al. 2023). However, with multi-dimensional effects taken into account, we would expect a comparable number of high-velocity and normal-velocity SNe Ia triggered by DDet. A substantial fraction of the objects within the clump on the $M_{B,\max}$-v_{Si} diagram, which has been proposed to consist of mostly near-M_{Ch} events, may turn out to be sub-M_{Ch} DDet events viewed from certain orientations (Shen et al. 2021b). SN 2018aoz, the DDet candidate with a suppress in B-band flux and excess emission in the infant phase light curve (Ni et al. 2022), which also lies in the clump in the $M_{B,\max}$-v_{Si} space at maximum brightness (Ni et al. 2023), may be another example of DDet SN Ia viewed from the hemisphere opposite to where the helium initially detonates.

In the bottom panels of Figure 6 we show three 2D DDet models with a total progenitor mass of $\sim 1\,M_\odot$ from Shen et al. (2021b), of which the predicted spectra at peak qualitatively match the observations. The $\rho_5 = 6$ model has a helium shell of $\sim 0.05\,M_\odot$. We find that when $\mu = 0$ (viewed from the equator), the model predicts a reasonable level of line blanketing in the blue side of the spectrum at early times. Near maximum brightness, the model also reproduces the overall shape of the observed spectrum, though overestimating the strengths of almost all absorption lines (4200 Å features, S II, and Si II). The line velocity of Si II λ ($\sim 12{,}000\,\mathrm{km\,s^{-1}}$) is also overestimated. When viewed from a hemisphere opposite to the helium detonation point (e.g., $\mu = -0.67$), the model yields an asymmetric profile of 4200 Å features as a blend of Ti II, Fe II, and Co II lines that matches the observations better. The Si II features are also predicted to be shallower, though still not as shallow as that in the observations. Nonetheless, the spectra at early times are expected to be much bluer than the observations. The $\rho_5 = 14$ model has a thicker helium shell ($\sim 0.1\,M_\odot$), and produces even shallower and slower-expanding Si II features at maximum

brightness, while the Ti II absorption is not sufficiently strong. The level of line-blanketing blueward of $\sim 5000\,\text{Å}$ is also underestimated at early times. In addition, all three models ($M_{B,\text{max}} \simeq -19.3\,\text{mag}$) are not as bright as SN 2022joj. Unfortunately, there are only two models in Shen et al. (2021b) that start from a progenitor more massive than $1\,\text{M}_\odot$, both with a thin helium shell ($\lesssim 0.01\,\text{M}_\odot$). Thus they cannot reproduce the red color at ~ -12 days or the remarkable $4200\,\text{Å}$ features at peak.

We draw the conclusions that the spectroscopic properties of SN 2022joj are qualitatively consistent with that of a sub-M_{Ch} WD ($\gtrsim 1.0\,\text{M}_\odot$) ignited by a relatively massive ($\sim 0.05\,\text{M}_\odot$) helium shell, viewed from the hemisphere opposite to where the shell detonates. Observers from such a viewing angle would observe strong absorption features in the blue portion of the spectrum dominated by Ti II and IGEs as well as relatively shallow and slowly-expanding Si II lines in the red portion. However, none of the individual models can reproduce all the features simultaneously, thus the DDet nature and the progenitor properties are still uncertain. This calls for a larger number of 2D DDet simulations covering a denser grid of model parameters. Dealing with the complications in radiative transfer (e.g., non-LTE effects; see Shen et al. 2021a) in a more realistic way is also of fundamental importance.

4.2. *The 7300 Å Region in Nebular-phase Spectra*

In Figure 7 we compare the two nebular-phase spectra of SN 2022joj with those of some overluminous SNe Ia (SN 1991T, SN 1999aa, and SN 2018cnw) and a normal SN Ia (SN 2011fe), where the flux has been normalized to the [Fe III] features around $4700\,\text{Å}$.

We mainly focus on the complex at $\sim 7300\,\text{Å}$ (here after the $7300\,\text{Å}$ features) that is usually dominated by [Fe II] and [Ni II], although in some peculiar SNe Ia, [Ca II] $\lambda\lambda 7291, 7324$ emissions are also detected (e.g., Siebert et al. 2020). Both spectra of SN 2022joj show relatively low flux ratio between the $7300\,\text{Å}$ features and the [Fe III] $4700\,\text{Å}$ features, compared to other SNe Ia. This suggests high ionization in the ejecta (Wilk et al. 2020). The profile of the $7300\,\text{Å}$ features in SN 2022joj is also distinct from others. Most of SNe Ia show a bimodal structure in their $7300\,\text{Å}$ features (e.g., Graham et al. 2017; Maguire et al. 2018). The bluer peak is dominated by [Fe II] $\lambda\lambda 7155, 7172$, while [Ni II] $\lambda\lambda 7378, 7412$ usually have non-negligible contributions to the redder peak (see Figure 7). The bimodal morphology is prominent in the spectra of SN 1999aa and SN 2011fe. SN 1999T is well-known for its broader emission lines in the nebular phase, so the composition of the $7300\,\text{Å}$ features is ambiguous. In the spectra of SN 2022joj and SN 2018cnw,

however, the redder peak is absent and the $7300\,\text{Å}$ features show an asymmetric single peak, which seems to indicate a low abundance of Ni in the ejecta.

To investigate the relative contributions of [Fe II] and [Ni II] to the $7300\,\text{Å}$ features in SN 2022joj, we model this region with multiple Gaussian emission profiles using the same techniques in modeling absorption lines (Section 3.3). We include four [Fe II] lines (7155, 7172, 7388, 7453 Å) and two [Ni II] lines (7378, 7412 Å) in the fit. For each species, the relative flux ratios of lines are fixed, whose values are adopted from Jerkstrand et al. (2015). For [Fe II], we set $L_{7155} : L_{7172} : L_{7388} : L_{7453} = 1 : 0.24 : 0.19 : 0.31$, and for [Ni II], we set $L_{7378} : L_{7412} = 1 : 0.31$. These line ratios are calculated assuming LTE, but the departure from LTE should not be significant under the typical conditions in the ejecta (Jerkstrand et al. 2015). We allow the amplitudes of these Gaussian profiles to be either positive or negative. The velocity dispersions in different lines of each species are set to be the same. The fitted models are shown in Figure 8, where colored curves correspond to the [Fe II] and [Ni II] emission adopting the mean values of the posterior distributions of model parameters sampled with MCMC. In both spectra, the flux of [Ni II] is consistent with 0 ($L_{\text{Ni II}}/L_{\text{Fe II}} = 0.04 \pm 0.11$ at $+286$ days and 0.07 ± 0.11 at $+329$ days; the flux ratios of lines are estimated with the ratios of their pEWs), and the $7300\,\text{Å}$ features can be well fit with [Fe II] emission only. There is no evidence for [Ca II] emission either.

The flux ratios of the emission lines can be used to estimate the relative abundance between Ni and Fe, which is a probe of the potential progenitor system. Over one year after the explosion, the dominant isotope of Fe is the stable ^{56}Fe as the products of ^{56}Ni through the chain: $^{56}\text{Ni} \rightarrow {}^{56}\text{Co} \rightarrow {}^{56}\text{Fe}$. Consequently, the Fe abundance essentially depends on the yields of ^{56}Ni, which is similar among different explosion scenarios and progenitor systems as long as the resultant SNe show a maximum brightness. The Ni abundance, however, are sensitive to both progenitor mass and explosion scenario. The stable Ni isotopes (^{58}Ni, ^{60}Ni, and ^{62}Ni) are more neutron-rich compared to the α-species ^{56}Ni, and can only be formed in high-density regions with a enhanced electron capture rate during the explosion (Nomoto 1984; Khokhlov 1991). Consequently, SNe Ia from sub-M_{Ch} WDs, whose central densities are lower than that of near-M_{Ch} WDs, are expected to show a lower abundance of stable Ni isotopes (Iwamoto et al. 1999; Seitenzahl et al. 2013; Shen et al. 2018).

To estimate the relative abundance of Ni and Fe, we use the equation adopted in Jerkstrand et al. (2015) and
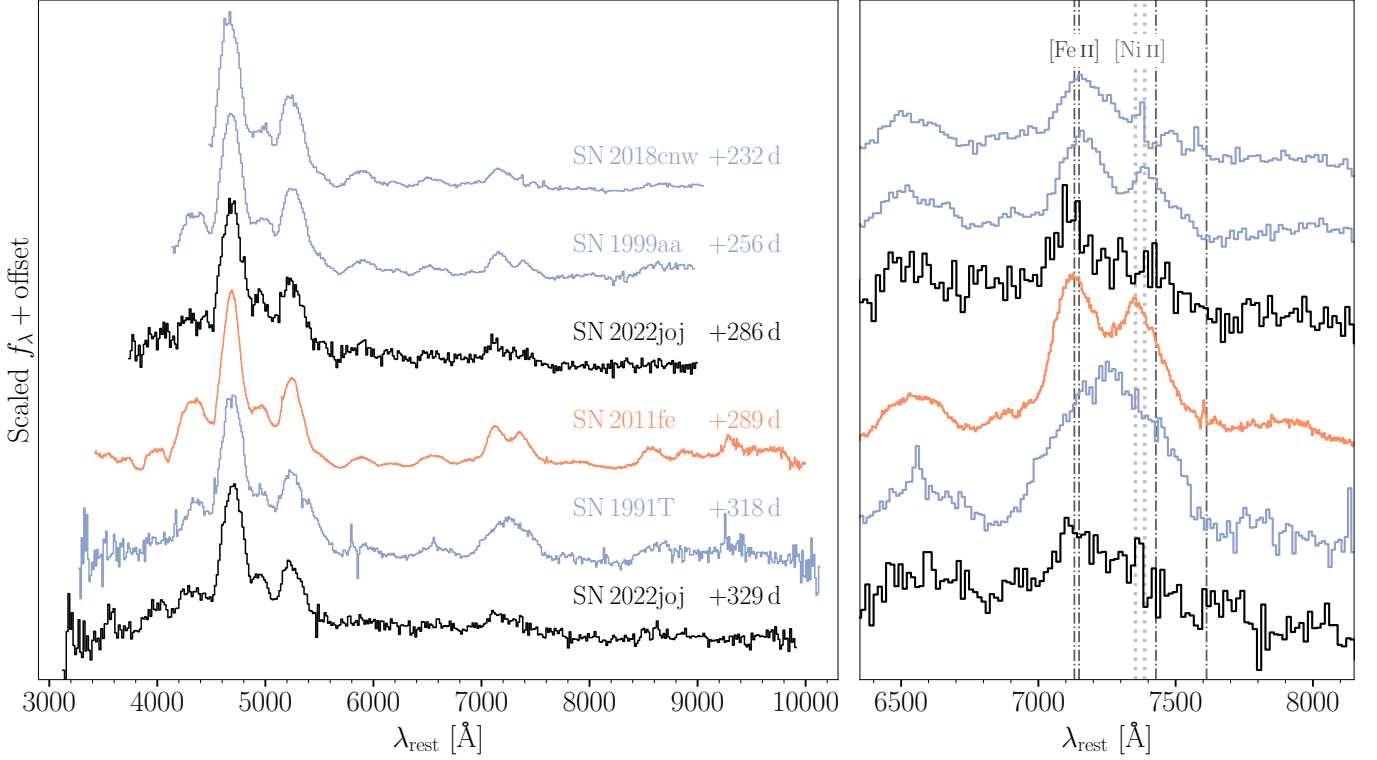
Figure 7. Nebular-phase spectra of SN 2022joj (black), three overluminous SNe Ia (blue), SN 1991T, SN 1999aa, and SN 2018cnw, and a normal SN Ia (orange), SN 2011fe. The right panel zooms in on the features around 7300 Å. The flux has been normalized to the [Fe III] features around 4700 Å. The dash-dotted lines correspond to wavelengths of four [Fe II] lines (7155 Å, 7172 Å, 7453 Å, and 7638 Å), while the dotted lines correspond to the wavelengths of two [Ni II] lines (7378 Å, 7412 Å), both blueshifted by 1000 km s^{-1}.
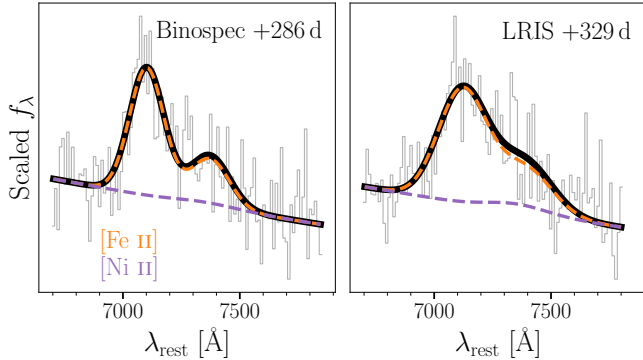
Figure 8. Fits to the 7300 Å region containing [Fe II] and [Ni II] features are consistent with a low Ni II abundance. The observed spectra are shown in grey. The dashed lines correspond to the models of [Fe II] (orange) and [Ni II] (purple) features. For the model parameters we adopt the mean values of their posterior distributions. The black solid lines are the overall models.

Maguire et al. (2018),

$$\frac{L_{7378}}{L_{7155}} = 4.9 \frac{n_{\mathrm{Ni\,II}}}{n_{\mathrm{Fe\,II}}} \exp\left(\frac{0.28\,\mathrm{eV}}{k_B T}\right) \frac{dc_{\mathrm{Ni\,II}}}{dc_{\mathrm{Fe\,II}}}, \qquad (1)$$

where L_{7378}/L_{7155} is the flux ratio of the [Ni II] λ7378 to [Fe II] λ7155 lines, $n_{\mathrm{Ni\,II}}$ ($n_{\mathrm{Fe\,II}}$) is the number density of Ni II (Fe II), and $dc_{\mathrm{Ni\,II}}/dc_{\mathrm{Fe\,II}}$ is the ratio of the departure coefficients from LTE for these two ions. Since both Ni II and Fe II are singly ionized species with similar ionization potentials, we assume that $n_{\mathrm{Ni\,II}}/n_{\mathrm{Fe\,II}}$ is a good approximation of the total Ni/Fe ratio. As is illustrated in Maguire et al. (2018), this assumption proves to be valid by modeling nebular phase spectra at similar phases (Fransson & Jerkstrand 2015; Shingles et al. 2022), with the relative deviation from the ionization balance $\lesssim 20\%$. We handle the uncertainties due to the unknown temperature, ratio of departure coefficients, and the ionization balance in a Monte Carlo way. We randomly generate $N = 4000$ samples of the temperature (3000–8000 K), the ratio of departure coefficients (1.2–2.4), and the ionization balance factor (0.8–1.2) assuming uncorrelated uniform distributions. These intervals are again adopted from Maguire et al. (2018). Combining these quantities with the samples of line profile parameters drawn with the MCMC, we obtain N estimates of Ni/Fe, which are effectively drawn from its posterior distribution. The mean value of Ni/Fe is $\sim$0.004, and a 3-σ upper limit of $\sim$0.026 is placed.

Such a low Ni abundance is more consistent with the yields of sub-$M_{\rm Ch}$ DDet scenarios (Shen et al. 2018), much lower than the expected outcomes of near-$M_{\rm Ch}$, delayed detonation models (Seitenzahl et al. 2013) or pure deflagration models (Iwamoto et al. 1999).

We also find that the [Fe II] lines are significantly blueshifted ($v_{\rm [Fe\,II]} = -2.36 \pm 0.35\,{\rm km\,s^{-1}}$ at $+286$ days and $-1.52 \pm 0.51\,{\rm km\,s^{-1}}$ at $+329$ days). This is consistent with other SNe Ia showing low $v_{\rm Si}$ at maximum brightness (Maeda et al. 2010; Maguire et al. 2018; Li et al. 2021), and also in qualitative agreement with the asymmetric sub-$M_{\rm Ch}$ DDet scenarios. Specifically, along a line of sight opposite to the shell detonation point, observers would see intermediate mass elements (IMEs) with low expansion velocities, including Si II. In the meantime, the IGEs at the center of the ejecta would have a bulk velocity towards the observer (Fink et al. 2010; Bulla et al. 2016).

5. CONCLUSIONS

Facility: PO:1.2m (ZTF), PO:1.5m (SEDM), FTN (FLOYDS), FTS (FLOYDS), NOT (ALFOSC), Liverpool:2m (SPRAT), Keck:I (LRIS), MMT (Binospec).

Software: astropy (Astropy Collaboration et al. 2013, 2018), matplotlib (Hunter 2007), NumPy (Harris et al. 2020), PyMC (Salvatier et al. 2016), PypeIt (Prochaska et al. 2020), pysedm (Rigault et al. 2019), SALT3 (Kenworthy et al. 2021), sncosmo (Barbary et al. 2023),

REFERENCES

Arbour, R., Papenkova, M., Li, W. D., Filippenko, A. V., & Armstrong, M. 1999, IAUC, 7156, 1

Astropy Collaboration, Robitaille, T. P., Tollerud, E. J., et al. 2013, A&A, 558, A33, doi: 10.1051/0004-6361/201322068

Astropy Collaboration, Price-Whelan, A. M., Sipőcz, B. M., et al. 2018, AJ, 156, 123, doi: 10.3847/1538-3881/aabc4f

Barbary, K., Bailey, S., Barentsen, G., et al. 2023, SNCosmo, v2.10.0, Zenodo, doi: 10.5281/zenodo.7876632

Bellm, E. C., Kulkarni, S. R., Graham, M. J., et al. 2019a, PASP, 131, 018002, doi: 10.1088/1538-3873/aaecbe

Bellm, E. C., Kulkarni, S. R., Barlow, T., et al. 2019b, PASP, 131, 068003, doi: 10.1088/1538-3873/ab0c2a

Blagorodnova, N., Neill, J. D., Walters, R., et al. 2018, PASP, 130, 035003, doi: 10.1088/1538-3873/aaa53f

Blondin, S., & Tonry, J. L. 2007, ApJ, 666, 1024, doi: 10.1086/520494

Branch, D., Thomas, R. C., Baron, E., et al. 2004, ApJ, 606, 413, doi: 10.1086/382950

Branch, D., Dang, L. C., Hall, N., et al. 2006, PASP, 118, 560, doi: 10.1086/502778

Brown, T. M., Baliber, N., Bianco, F. B., et al. 2013, PASP, 125, 1031, doi: 10.1086/673168

Bulla, M., Sim, S. A., Kromer, M., et al. 2016, MNRAS, 462, 1039, doi: 10.1093/mnras/stw1733

Bulla, M., Miller, A. A., Yao, Y., et al. 2020, ApJ, 902, 48, doi: 10.3847/1538-4357/abb13c

Burrow, A., Baron, E., Ashall, C., et al. 2020, ApJ, 901, 154, doi: 10.3847/1538-4357/abafa2

Cao, Y., Kulkarni, S. R., Howell, D. A., et al. 2015, Nature, 521, 328, doi: 10.1038/nature14440

Carrick, J., Turnbull, S. J., Lavaux, G., & Hudson, M. J. 2015, MNRAS, 450, 317, doi: 10.1093/mnras/stv547

Cenko, S. B., Fox, D. B., Moon, D.-S., et al. 2006, PASP, 118, 1396, doi: 10.1086/508366

Chu, M., Dahiwale, A., & Fremling, C. 2022, Transient Name Server Classification Report, 2022-1458, 1

Deckers, M., Maguire, K., Magee, M. R., et al. 2022, MNRAS, 512, 1317, doi: 10.1093/mnras/stac558

Dekany, R., Smith, R. M., Riddle, R., et al. 2020, PASP, 132, 038001, doi: 10.1088/1538-3873/ab4ca2

Dey, A., Schlegel, D. J., Lang, D., et al. 2019, AJ, 157, 168, doi: 10.3847/1538-3881/ab089d

Dimitriadis, G., Maguire, K., Karambelkar, V. R., et al. 2023, MNRAS, 521, 1162, doi: 10.1093/mnras/stad536

Duev, D. A., Mahabal, A., Masci, F. J., et al. 2019, MNRAS, 489, 3582, doi: 10.1093/mnras/stz2357

Fabricant, D., Fata, R., Epps, H., et al. 2019, PASP, 131, 075004, doi: 10.1088/1538-3873/ab1d78

Filippenko, A. V., Richmond, M. W., Matheson, T., et al. 1992a, ApJL, 384, L15, doi: 10.1086/186252

Filippenko, A. V., Richmond, M. W., Branch, D., et al. 1992b, AJ, 104, 1543, doi: 10.1086/116339

Fink, M., Röpke, F. K., Hillebrandt, W., et al. 2010, A&A, 514, A53, doi: 10.1051/0004-6361/200913892

Fitzpatrick, E. L. 1999, PASP, 111, 63, doi: 10.1086/316293

Fransson, C., & Jerkstrand, A. 2015, ApJL, 814, L2, doi: 10.1088/2041-8205/814/1/L2

Fremling, C. 2022, Transient Name Server Discovery Report, 2022-1220, 1

Garavini, G., Folatelli, G., Goobar, A., et al. 2004, AJ, 128, 387, doi: 10.1086/421747

Graham, M. J., Kulkarni, S. R., Bellm, E. C., et al. 2019, PASP, 131, 078001, doi: 10.1088/1538-3873/ab006c

Graham, M. L., Kumar, S., Hosseinzadeh, G., et al. 2017, MNRAS, 472, 3437, doi: 10.1093/mnras/stx2224

Harris, C. R., Millman, K. J., van der Walt, S. J., et al. 2020, Nature, 585, 357, doi: 10.1038/s41586-020-2649-2

Hosseinzadeh, G., Sand, D. J., Valenti, S., et al. 2017, ApJL, 845, L11, doi: 10.3847/2041-8213/aa8402

Hunter, J. D. 2007, Computing in Science and Engineering, 9, 90, doi: 10.1109/MCSE.2007.55

Iwamoto, K., Brachwitz, F., Nomoto, K., et al. 1999, ApJS, 125, 439, doi: 10.1086/313278

Jerkstrand, A., Smartt, S. J., Sollerman, J., et al. 2015, MNRAS, 448, 2482, doi: 10.1093/mnras/stv087

Jiang, J.-a., Doi, M., Maeda, K., et al. 2017, Nature, 550, 80, doi: 10.1038/nature23908

Jiang, J.-a., Maeda, K., Kawabata, M., et al. 2021, ApJL, 923, L8, doi: 10.3847/2041-8213/ac375f

Kenworthy, W. D., Jones, D. O., Dai, M., et al. 2021, ApJ, 923, 265, doi: 10.3847/1538-4357/ac30d8

Khokhlov, A. M. 1991, A&A, 245, L25

Leibundgut, B., Kirshner, R. P., Phillips, M. M., et al. 1993, AJ, 105, 301, doi: 10.1086/116427

Li, W., Wang, X., Bulla, M., et al. 2021, ApJ, 906, 99, doi: 10.3847/1538-4357/abc9b5

Lira, P. 1996, Master's thesis, -

Liu, C., Miller, A. A., Polin, A., et al. 2023, ApJ, 946, 83, doi: 10.3847/1538-4357/acbb5e

Maeda, K., Benetti, S., Stritzinger, M., et al. 2010, Nature, 466, 82, doi: 10.1038/nature09122

Magee, M. R., & Maguire, K. 2020, A&A, 642, A189, doi: 10.1051/0004-6361/202037870

Maguire, K., Sim, S. A., Shingles, L., et al. 2018, MNRAS, 477, 3567, doi: 10.1093/mnras/sty820

Mahabal, A., Rebbapragada, U., Walters, R., et al. 2019, PASP, 131, 038002, doi: 10.1088/1538-3873/aaf3fa

Marion, G. H., Brown, P. J., Vinkó, J., et al. 2016, ApJ, 820, 92, doi: 10.3847/0004-637X/820/2/92

Masci, F. J., Laher, R. R., Rusholme, B., et al. 2019, PASP, 131, 018003, doi: 10.1088/1538-3873/aae8ac

Matheson, T., Filippenko, A. V., Barth, A. J., et al. 2000, AJ, 120, 1487, doi: 10.1086/301518

Matheson, T., Kirshner, R. P., Challis, P., et al. 2008, AJ, 135, 1598, doi: 10.1088/0004-6256/135/4/1598

Mazzali, P. A., Chugai, N., Turatto, M., et al. 1997, MNRAS, 284, 151, doi: 10.1093/mnras/284.1.151

Miller, A. A., Yao, Y., Bulla, M., et al. 2020, ApJ, 902, 47, doi: 10.3847/1538-4357/abb13b

Newsome, M., Li, W., Burke, J., et al. 2022, Transient Name Server Classification Report, 2022-1274, 1

Ni, Y. Q., Moon, D.-S., Drout, M. R., et al. 2022, Nature Astronomy, 6, 568, doi: 10.1038/s41550-022-01603-4

—. 2023, ApJ, 946, 7, doi: 10.3847/1538-4357/aca9be

Nomoto, K. 1984, ApJ, 277, 791, doi: 10.1086/161749

Nugent, A. E., Polin, A. E., & Nugent, P. E. 2023, arXiv e-prints, arXiv:2304.10601, doi: 10.48550/arXiv.2304.10601

Oke, J. B., Cohen, J. G., Carr, M., et al. 1995, PASP, 107, 375, doi: 10.1086/133562

Patterson, M. T., Bellm, E. C., Rusholme, B., et al. 2019, PASP, 131, 018001, doi: 10.1088/1538-3873/aae904

Pereira, R., Thomas, R. C., Aldering, G., et al. 2013, A&A, 554, A27, doi: 10.1051/0004-6361/201221008

Phillips, M. M., Lira, P., Suntzeff, N. B., et al. 1999, AJ, 118, 1766, doi: 10.1086/301032

Piascik, A. S., Steele, I. A., Bates, S. D., et al. 2014, in Society of Photo-Optical Instrumentation Engineers (SPIE) Conference Series, Vol. 9147, Ground-based and Airborne Instrumentation for Astronomy V, ed. S. K. Ramsay, I. S. McLean, & H. Takami, 91478H, doi: 10.1117/12.2055117

Piro, A. L., & Morozova, V. S. 2016, ApJ, 826, 96, doi: 10.3847/0004-637X/826/1/96

Piro, A. L., & Nakar, E. 2013, ApJ, 769, 67, doi: 10.1088/0004-637X/769/1/67

Polin, A., Nugent, P., & Kasen, D. 2019, ApJ, 873, 84, doi: 10.3847/1538-4357/aafb6a

Prochaska, J. X., Hennawi, J. F., Westfall, K. B., et al. 2020, Journal of Open Source Software, 5, 2308, doi: 10.21105/joss.02308

Prochaska, J. X., Hennawi, J., Cooke, R., et al. 2020, pypeit/PypeIt: Release 1.0.0, v1.0.0, Zenodo, doi: 10.5281/zenodo.3743493

Rigault, M., Neill, J. D., Blagorodnova, N., et al. 2019, A&A, 627, A115, doi: 10.1051/0004-6361/201935344

Salvatier, J., Wiecki, T. V., & Fonnesbeck, C. 2016, PeerJ Computer Science, 2, e55, doi: 10.7717/peerj-cs.55

Schlafly, E. F., & Finkbeiner, D. P. 2011, ApJ, 737, 103, doi: 10.1088/0004-637X/737/2/103

Seitenzahl, I. R., Ciaraldi-Schoolmann, F., Röpke, F. K., et al. 2013, MNRAS, 429, 1156, doi: 10.1093/mnras/sts402

Shen, K. J., Blondin, S., Kasen, D., et al. 2021a, ApJL, 909, L18, doi: 10.3847/2041-8213/abe69b

Shen, K. J., Boos, S. J., Townsley, D. M., & Kasen, D. 2021b, ApJ, 922, 68, doi: 10.3847/1538-4357/ac2304

Shen, K. J., Kasen, D., Miles, B. J., & Townsley, D. M. 2018, ApJ, 854, 52, doi: 10.3847/1538-4357/aaa8de

Shingles, L. J., Flörs, A., Sim, S. A., et al. 2022, MNRAS, 512, 6150, doi: 10.1093/mnras/stac902

Siebert, M. R., Dimitriadis, G., Polin, A., & Foley, R. J.
    2020, ApJL, 900, L27, doi: 10.3847/2041-8213/abae6e

Silverman, J. M., Foley, R. J., Filippenko, A. V., et al.
    2012, MNRAS, 425, 1789,
    doi: 10.1111/j.1365-2966.2012.21270.x

Steele, I. A., Smith, R. J., Rees, P. C., et al. 2004, in
    Society of Photo-Optical Instrumentation Engineers
    (SPIE) Conference Series, Vol. 5489, Ground-based
    Telescopes, ed. J. Oschmann, Jacobus M., 679–692,
    doi: 10.1117/12.551456

Taubenberger, S. 2017, in Handbook of Supernovae, ed.
    A. W. Alsabti & P. Murdin (Springer), 317,
    doi: 10.1007/978-3-319-21846-5_37

Wilk, K. D., Hillier, D. J., & Dessart, L. 2020, MNRAS,
    494, 2221, doi: 10.1093/mnras/staa640

Yao, Y., Miller, A. A., Kulkarni, S. R., et al. 2019, ApJ,
    886, 152, doi: 10.3847/1538-4357/ab4cf5

Yaron, O., & Gal-Yam, A. 2012, PASP, 124, 668,
    doi: 10.1086/666656

Zackay, B., Ofek, E. O., & Gal-Yam, A. 2016, ApJ, 830, 27,
    doi: 10.3847/0004-637X/830/1/27

Zheng, W., Kelly, P. L., & Filippenko, A. V. 2018, ApJ,
    858, 104, doi: 10.3847/1538-4357/aabaeb